Optics Letters

Filtering for unwrapping noisy Doppler optical coherence tomography images for extended microscopic fluid velocity measurement range

Yang Xu,[1,2,3] Donald Darga,[3] Jason Smid,[3] Adam M. Zysk,[3] Daniel Teh,[4] Stephen A. Boppart,[1,2,3,5] and P. Scott Carney[1,2,3,*]

[1]Beckman Institute for Advanced Science and Technology, University of Illinois at Urbana-Champaign, 405 North Mathews Avenue, Urbana, Illinois 61801, USA
[2]Department of Electrical and Computer Engineering, University of Illinois at Urbana-Champaign, 306 North Wright Street, Urbana, Illinois 61801, USA
[3]Diagnostic Photonics, Inc., 222 Merchandise Mart Plaza, Suite 1230, Chicago, Illinois 60654, USA
[4]Department of Computer Science, University of Illinois at Urbana-Champaign, 201 North Goodwin Avenue, Urbana, Illinois 61801, USA
[5]Department of Bioengineering, University of Illinois at Urbana-Champaign, 1304 West Springfield Avenue, Urbana, Illinois 61801, USA
*Corresponding author: Carney@illinois.edu

In this Letter, we report the first application of two phase denoising algorithms to Doppler optical coherence tomography (DOCT) velocity maps. When combined with unwrapping algorithms, significantly extended fluid velocity dynamic range is achieved. Instead of the physical upper bound, the fluid velocity dynamic range is now limited by noise level. We show comparisons between physical simulated ideal velocity maps and the experimental results of both algorithms. We demonstrate unwrapped DOCT velocity maps having a peak velocity nearly 10 times the theoretical measurement range. © 2016 Optical Society of America

OCIS codes: (110.4500) Optical coherence tomography; (170.3340) Laser Doppler velocimetry; (100.2000) Digital image processing.

Doppler optical coherence tomography (DOCT) [1–4] is an optical coherence tomography (OCT) [5,6]–based technique for microscopic velocity measurement in a sample, usually a scattering fluid. Inherited from OCT, DOCT is a noninvasive imaging modality that generates depth-resolved velocity maps with micron-scale resolution. Its near-infrared light beam can penetrate through several millimeters of biological tissue, which makes it especially useful for biomedical applications such as blood flow monitoring [1–3].

Doppler OCT acquires data with transverse spatial oversampling so that any two consecutive axial scans (A-scans) measure effectively the same part of the sample. Each A-scan is acquired with a fixed time-step T. An element of the sample in motion along the optical axis (A-scan direction) causes an apparent phase shift between subsequent A-scans. The phase difference at a given axial depth z and lateral scan position x is given by $\Delta\phi(x,z) = \phi(x,z) - \phi(x+1,z)$, and the flow velocity $V(x,z) = \Delta\phi(x,z)\lambda/(4\pi nT \cos \alpha)$ is proportional to the phase difference [4], where λ is the system center wavelength, n is the fluid refractive index, T is the A-scan interval, and α is the angle between the flow direction and the cross-sectional plane being measured.

Because of the 2π ambiguity brought by the numerical difference of phase, a DOCT system can only measure velocity within a range $[-V_{\max}, +V_{\max}]$ [4], where

$$V_{\max} = \frac{\lambda}{4nT \cos \alpha}. \qquad (1)$$

Any velocity outside of this range will appear modulo $2V_{\max}$ into the range, because of phase wrapping. This usually limits the use of DOCT in larger blood vessels with higher velocity, such as the carotid artery [7].

Velocity wrapping in DOCT has been previously reported [8–10], but unwrapping was not carried out in these studies because of the difficulty brought by noise in the velocity map. Successful attempts have been reported [7,11–13] using cellular automata [14] or quality-guided 2D unwrapping algorithms [15] to achieve an unwrapping of peak velocity up to $7.5V_{\max}$ without incorporating noise rejection in the algorithm. Another algorithm, synthetic wavelengths [16–18], also achieved successful OCT (axial height) and DOCT unwrapping by splitting the spectrum and synthesizing an OCT image acquired by a much shorter wavelength.

The obstacle to unwrapping noisier and higher-velocity maps usually lies in the lack of effective denoising algorithms. Note that spatial low-pass filters are not suitable in this case because they smooth out the $-V_{\max}$ to $+V_{\max}$ jumps; as a result, the unwrapping algorithm is unable to detect the edge of a wrap. Similarly, for spatial median filters at $-V_{\max}$ to $+V_{\max}$ jumps, they will likely reject the values close to $-V_{\max}$ or $+V_{\max}$ and pick up noise with an intermediate value. More advanced wrapped-phase filtering algorithms [19–21] have been developed or used by communities studying radar,

shearography, digital holography, etc. We selected two algorithms and adapted them for filtering DOCT velocity maps.

For DOCT data with a low peak velocity and moderate noise, we propose to use the sine/cosine average filter (SCAF) [20]. This method is simpler and faster than the second method below. For the noisy wrapped phase difference $\Delta\phi(x, z)$, we calculate its pixel-wise sine and cosine, $P(x, z) = \sin(\Delta\phi(x, z))$, $Q(x, z) = \cos(\Delta\phi(x, z))$. After the transformation, the $-\pi$ and $+\pi$ jumps become spatially continuous in value, and thus will not be negatively affected by filtering. Therefore, spatial low-pass filters and median filters can be applied to P and Q for denoising. Denoting the filtered version as P_f and Q_f, the filtered velocity map can be recovered by $V_f(x, z) = V_{\max} \arctan(P_f(x, z)/Q_f(x, z))/\pi$, with the four-quadrant inverse tangent function used here. This filter can be reapplied as necessary for better results [20]. After filtering and velocity recovery, direct or quality-guided unwrapping can be applied to the image to obtain the full-range velocity map. This method is easy to implement, computationally inexpensive, and works well for datasets with moderate noise and wrapping.

For highly wrapped or relatively noisier DOCT datasets, we use a more robust method (denoted by the "phase tracker method" below) for data denoising, inspired by the regularized phase tracker (RPT) method [19]. Compared to the RPT method, our method uses a simplified cost function without the regularization term so that there is no interdependence of output data. This makes it suitable for implementation on parallel computing platforms. This method assumes that the fluid is incompressible, is irrotational, and obeys mass conservation (is source-free). It relies on the fluid dynamics principle that velocity is continuous everywhere within a flow. The method extracts information and rejects noise by taking advantage of the spatial correlation and redundancy of nearby pixels.

The "phase tracker method," which is illustrated in Fig. 1, is as follows. For each pixel (x_0, z_0) in the velocity map, a sliding window $\Delta\phi^{\mathrm{win}}_{(x_0, z_0)}(x, z) = \Delta\phi(x_0 + x, z_0 + z)$, $|x| \leq a, |z| \leq a$ of preset size $(2a + 1$ by $2a + 1$ pixels) is created around it. Depending on the application and noise level of the system, the window size should be large enough so that wavefronts may be identified under the noise in the window, but small
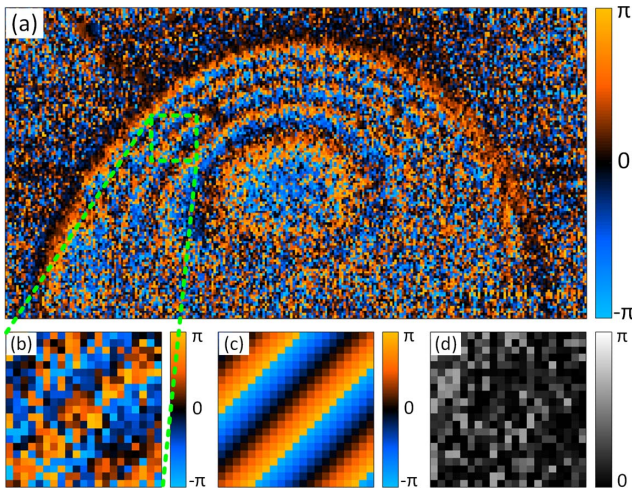
enough that the wavefronts may be assumed locally flat. The objective is to fit the window using three free parameters, the horizontal and vertical spatial frequencies (w_x, w_z), and a DC offset ϕ_0, $\Delta\phi^{\mathrm{fit}}_{(x_0, z_0)}(x, z) = \omega_x x + \omega_z z + \phi_0$, $|x| \leq a, |z| \leq a$. The optimum fit is found through minimizing the cost function $E_{(x_0, z_0)}$ over the three free parameters

$$[\hat{w}_x, \hat{w}_z, \hat{\phi}_0] = \arg \min_{(w_x, w_z, \phi_0)} E_{(x_0, z_0)}(w_x, w_z, \phi_0), \quad \textbf{(2)}$$
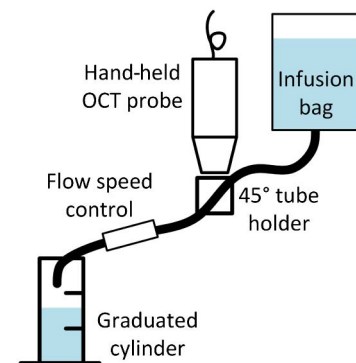
where the cost function minimizes the sum of the weighted l^2 error between the sine and cosine value of the window and the fit,

$$
\begin{aligned}
&E_{(x_0, z_0)}(w_x, w_z, \phi_0) \\
&= \sum_{|x| \leq a, |z| \leq a} G(x, z) \\
&\quad \times [|\cos(\Delta\phi^{\mathrm{win}}_{(x_0, z_0)}(x, z)) - \cos(\Delta\phi^{\mathrm{fit}}_{(x_0, z_0)}(x, z))|^2 \\
&\quad + |\sin(\Delta\phi^{\mathrm{win}}_{(x_0, z_0)}(x, z)) - \sin(\Delta\phi^{\mathrm{fit}}_{(x_0, z_0)}(x, z))|^2], \quad \textbf{(3)}
\end{aligned}
$$

where $G(x, z)$ is an optional Gaussian weighting mask that emphasizes error in the center part of the window. The original RPT algorithm [19] uses gradient descent to optimize the cost function, which comes with the risk of becoming stuck in the many local minima of this cost function. We chose the slower but safer option of exhaustive search and used parallel processing to mitigate the speed issue. After optimization, the center pixel of the window in the filtered image $S_{\mathrm{filtered}}(x_0, z_0)$ takes the value of the optimum $\hat{\phi}_0$ of the corresponding window. Finally, after the filtering step, the filtered velocity map is mostly noise free and can be unwrapped directly or using a quality-guided unwrapping method.

DOCT imaging experiments and physical-model-based simulations were conducted to validate the algorithm. In the experiment, an OCT probe was used to measure the velocity map of diluted milk flowing through a tube. As shown in Fig. 2, the fluid flowed from an infusion bag through a plastic tube (PVC, 1.6 mm inner diameter) into a graduated cylinder. The flow rate was controlled using a pinch clip located at the lower end of the tube. The average flow rate Q_{avg} was calculated by dividing the volume change in the graduated cylinder over time.

The system used in the experiment is a swept-source OCT imaging system (Diagnostic Photonics, Inc.) operating at a center wavelength of 1310 nm, with a spectral bandwidth of 100 nm, an A-scan rate of 50 kHz, and an imaging aperture of 0.043 NA. The transverse resolution is 11.5 μm FWHM. The system scans with 4x oversampling at 3 μm step size. The maximum measurable velocity at 45° in diluted

Fig. 1. Illustration of the stages in the "phase tracker method." (a) A window is chosen. (b) Windowed data are fit to a plane wave. (c) Error is computed.

Fig. 2. Schematic of the experimental setup.

milk is $V_{max} = 1.75$ cm/s. Beyond this velocity, the wrapping is manifest. Each dataset has an estimated average signal-to-noise ratio (SNR) of 12.8 dB and a peak SNR (PSNR) of 34.5 dB.

To provide a ground truth for comparison, we performed noiseless simulations using the simple model of laminar flow in cylindrical tubes [22] to estimate the true cross-sectional flow velocity map. When the average flow velocity $V_{avg} = Q_{avg}/A_{tube}$ is known, the cross-sectional velocity map can be modeled as $V(\rho) = 2V_{avg}(1 - \rho^2/r^2)$ where r is the inner-radius of the tube, and ρ is the radius variable of the polar coordinate system, with a range of $0 \leq \rho \leq r$. According to this model, the fluid velocity at the inner wall of the tube is 0, and the velocity at the center is $2V_{avg}$. Note that the noiseless simulations serve only as a ground truth for comparison and hence are not for demonstration of the denoising or unwrapping algorithms.

Experimental datasets were processed using both algorithms—each using the same set of parameters—combined with a simple one-dimensional phase unwrapping algorithm. Because the original velocity maps contain too much noise, direct unwrapping produces unusable results, which are not shown. Figure 3 shows a comparison of the simulations and the experimental results processed by the SCAF method. In this case, the SCAF method works well for relatively low peak velocities in the range of 0–5 multiples of V_{max}. Striping artifacts gradually appear as the velocity exceeds this range. Three datasets with a more challenging range of velocities processed by the "phase tracker method" are shown in Fig. 4. It can be seen that

the "phase tracker method" generates a much smoother velocity gradient from the noisy raw data, and the results agree well with the physically simulated velocity profile. The "phase tracker method" is computationally more expensive compared to the SCAF method, but its performance in highly noisy and highly wrapped datasets makes it desirable for the more challenging scenarios, e.g., in this case a peak velocity over $5V_{max}$.

In our implementation, the "phase tracker method" is implemented in CUDA for faster processing on a graphics processing unit (GPU). Because of the modification on the original RPT that eliminates the interdependence between output pixels, the massively parallel floating point computation capability of the graphics card can be fully utilized by splitting the workload (pixels and optimization dimensions) onto the CUDA cores. With some optimization, each DOCT dataset can be filtered and unwrapped in around 3 s, with the average single precision floating point throughput (FP32) reaching 800–1200 GFLOPS, which is 60%–90% of the theoretical peak performance of the nVidia GeForce GTX 750 Ti GPU (nVidia, Inc.).

In this Letter, we present two methods for filtering noisy wrapped DOCT velocity maps. The filtered image can then be unwrapped with much less error, which essentially extends the measurable velocity range of a DOCT system. The SCAF method uses a sine/cosine transformation to enable the use of low-pass filters and median filters for noise rejection. The "phase tracker method" searches for the best fit of the phase through an optimization process to extract information mixed in noise. By comparing the physical simulation and the unwrapped results,
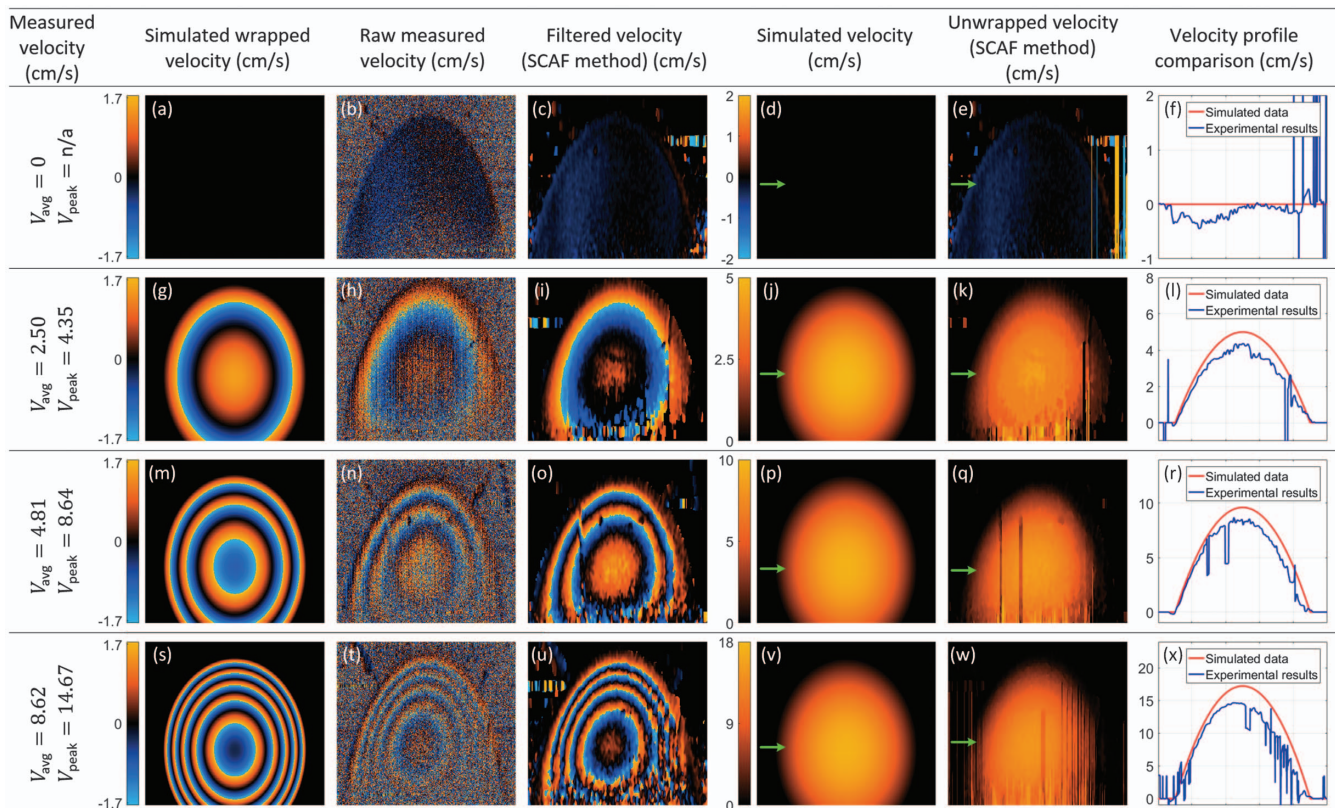
Fig. 3. Array of images shows a comparison of the simulation and experimental results using the SCAF method. The average velocities of the datasets are (a)–(f) 0 cm/s, (g)–(l) 2.50 cm/s, (m)–(r) 4.81 cm/s, and (s)–(x) 8.62 cm/s. The measured peak velocities range from 0 to $8.4V_{max}$. The velocity profiles were taken at the depth labeled by green arrows. It can be seen that the SCAF method works well for lower velocities and gradually starts to break when peak velocities are between 8.64 and 14.67 cm/s.
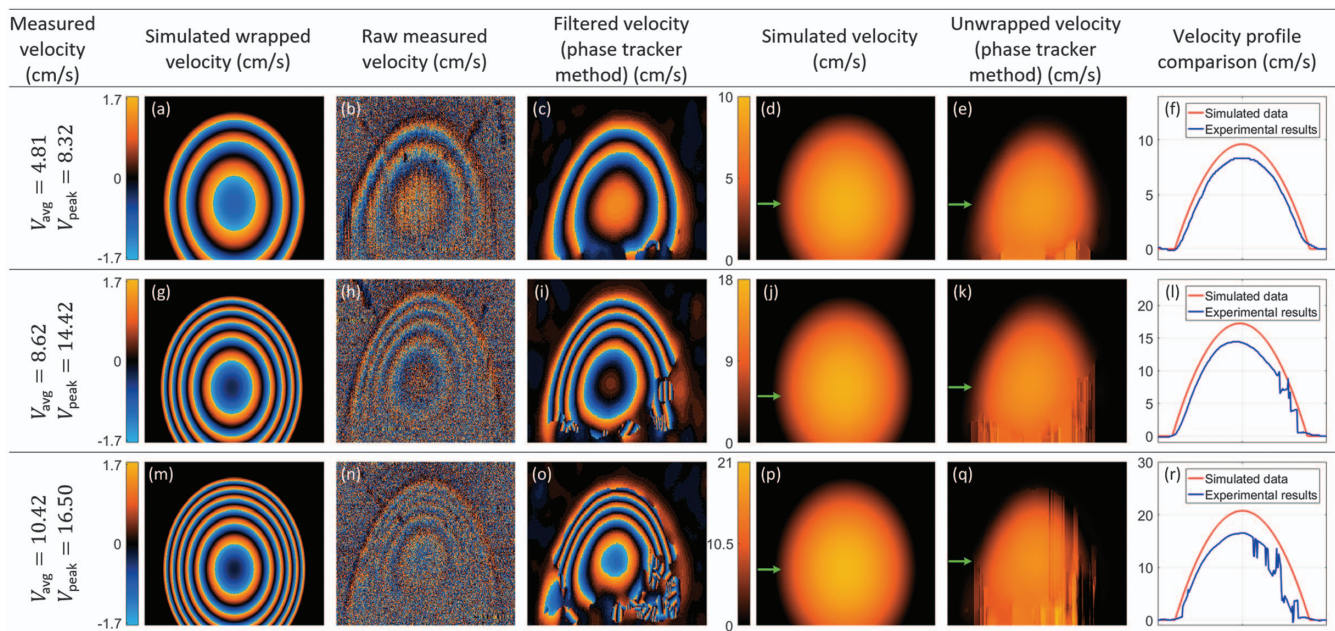
Fig. 4. Array of images shows a comparison of the simulation and experimental results using the "phase tracker method." The average velocities of the datasets are (a)–(f) 4.81 cm/s, (g)–(l) 8.62 cm/s, and (m)–(r) 10.42 cm/s. The peak velocities range from 8.32 to 16.50 cm/s ($4.8V_{\max}$–$9.4V_{\max}$). The velocity profiles were taken at the depth labeled by green arrows. It can be seen that this method generates smooth and nearly noise-free velocity maps that agree well with the physical model.

the validity and performance of both methods are demonstrated. While the "phase tracker method" requires more computation per pixel, we have shown that the process can be significantly shortened by implementation in a parallel processing architecture, making semi-real-time processing possible. Because this Letter focuses on the denoising aspect, a simple one-dimensional unwrapping algorithm is used. However, if combined with more advanced two-dimensional unwrapping algorithms, such as quality-guided unwrapping, it should be capable of unwrapping even more challenging DOCT velocity maps. It should be noted that both algorithms, while effective in denoising, also inevitably cause the loss of details in the images. The filter parameters or the window size should be carefully chosen to balance the trade-off to suit the intended applications.

REFERENCES

1. J. A. Izatt, M. D. Kulkarni, S. Yazdanfar, J. K. Barton, and A. J. Welch, Opt. Lett. **22**, 1439 (1997).
2. Y. Zhao, Z. Chen, C. Saxer, S. Xiang, J. F. de Boer, and J. S. Nelson, Opt. Lett. **25**, 114 (2000).
3. R. A. Leitgeb, L. Schmetterer, W. Drexler, A. Fercher, R. Zawadzki, and T. Bajraszewski, Opt. Express **11**, 3116 (2003).
4. R. A. Leitgeb, R. M. Werkmeister, C. Blatter, and L. Schmetterer, Prog. Retinal Eye Res. **41**, 26 (2014).
5. D. Huang, E. A. Swanson, C. P. Lin, J. S. Schuman, W. G. Stinson, W. Chang, M. R. Hee, T. Flotte, K. Gregory, C. A. Puliafito, and J. G. Fujimoto, Science **254**, 1178 (1991).
6. A. F. Fercher, J. Biomed. Opt. **1**, 157 (1996).
7. C. Sun, F. Nolte, K. H. Cheng, B. Vuong, K. K. Lee, B. A. Standish, B. Courtney, T. R. Marotta, A. Mariampillai, and V. X. Yang, Biomed. Opt. Express **3**, 2600 (2012).
8. V. Westphal, S. Yazdanfar, A. M. Rollins, and J. A. Izatt, Opt. Lett. **27**, 34 (2002).
9. V. Yang, M. Gordon, B. Qi, J. Pekar, S. Lo, E. Seng-Yue, A. Mok, B. Wilson, and I. Vitkin, Opt. Express **11**, 794 (2003).
10. A. Mariampillai, B. A. Standish, N. R. Munce, C. Randall, G. Liu, J. Y. Jiang, A. E. Cable, I. A. Vitkin, and V. X. Yang, Opt. Express **15**, 1627 (2007).
11. Y. Wang, B. A. Bower, J. A. Izatt, O. Tan, and D. Huang, J. Biomed. Opt. **12**, 041215 (2007).
12. Y. Wang, B. A. Bower, J. A. Izatt, O. Tan, and D. Huang, J. Biomed. Opt. **13**, 064003 (2008).
13. A. Davis, J. Izatt, and F. Rothenberg, Anat. Rec. **292**, 311 (2009).
14. D. C. Ghiglia, G. A. Mastin, and L. A. Romero, J. Opt. Soc. Am. A **4**, 267 (1987).
15. D. C. Ghiglia and M. D. Pritt, *Two-Dimensional Phase Unwrapping: Theory, Algorithms, and Software* (Wiley, 1998), Vol. 4.
16. H. C. Hendargo, M. Zhao, N. Shepherd, and J. A. Izatt, Opt. Express **17**, 5039 (2009).
17. H. C. Hendargo, R. P. McNabb, A.-H. Dhalla, N. Shepherd, and J. A. Izatt, Biomed. Opt. Express **2**, 2175 (2011).
18. J. Tokayer, Y. Jia, A.-H. Dhalla, and D. Huang, Biomed. Opt. Express **4**, 1909 (2013).
19. M. Servin, F. J. Cuevas, D. Malacara, J. L. Marroquin, and R. Rodriguez-Vera, Appl. Opt. **38**, 1934 (1999).
20. S. Waldner and N. Goudemand, in *Interferometry in Speckle Light: Theory and Applications*, P. Jacquot and J.-M. Fournier, eds. (Springer, 2000), Chap. 4, pp. 319–326.
21. K. J. Chalut, W. J. Brown, and A. Wax, Opt. Express **15**, 3047 (2007).
22. Y. Cengel and J. Cimbala, *Fluid Mechanics Fundamentals and Applications* (McGraw-Hill, 2013).